Infrared-induced ultrafast melting of nanostructured platinum films probed by an x-ray free-electron laser

Luca Gelisio,[1,*,†] Young Yong Kim,[1,‡] Seon Woo Lim,[2] Daewoong Nam,[3,4] Intae Eom,[3,4] Minseok Kim,[3] Sangsoo Kim,[3] Ruslan Khubbutdinov,[1] Li Xiang,[5] Hoyeol Lee,[5] Moonhor Ree,[3,5,6] Chae Un Kim,[2] and Ivan A. Vartanyants[1,§]

[1]*Photon Science, Deutsches Elektronen-Synchrotron DESY, Notkestraße 85, 22607 Hamburg, Germany*

[2]*Department of Physics, Ulsan National Institute of Science and Technology, 50 UNIST-gil, Ulju-gun, Ulsan 44919, Republic of Korea*

[3]*Pohang Accelerator Laboratory, Pohang University of Science and Technology, Pohang 37673, Republic of Korea*

[4]*Photon Science Center, Pohang University of Science and Technology, Pohang 37673, Republic of Korea*

[5]*Department of Chemistry, Pohang University of Science and Technology, Pohang 37673, Republic of Korea*

[6]*Surface Technology Institute, Ceko Corporation, 519 Dunchon-daero, Jungwon-gu, Seongnam 13216, Republic of Korea*

(Received 8 March 2023; revised 9 April 2024; accepted 13 September 2024; published 11 October 2024)

Understanding non-equilibrium melting in metals is a topic of current interest. We investigated the solid-to-liquid phase transition in platinum induced by femtosecond infrared radiation at different fluences. The evolution of the atomic structure was probed on the picoseconds timescale by x rays generated by an x-ray free-electron laser (XFEL). To analyze scattering data, we employed a model developed for liquid metals. We observed a compression field propagating into the nanostructured thin film sample, as well as partial melting for the infrared fluence of 200 mJ cm^{-2}, corresponding to about 280 kJ kg^{-1} absorbed by the sample. Similar features were observed at higher infrared laser fluences. To support the interpretation of experimental findings, we performed two-temperature model simulations.

DOI: 10.1103/PhysRevB.110.144303

I. INTRODUCTION

The nonequilibrium dynamics of the solid-liquid phase transition has been the subject of several investigations [1–7]. As a result, for instance, the transition from heterogeneous to homogeneous melting was identified in gold [4], and the role of grain boundaries elucidated [5]. In fact these, together with other defects, can act as nucleation seeds for the liquid phase, lowering the amount of energy required for the phase transition.

The solid-liquid phase transition can be induced, for example, employing infrared (IR) radiation emitted by a femtosecond laser to rapidly increase the kinetic energy of free electrons. During the IR pulse the energy of free electrons can exceed thousands of degrees Kelvin, while the atomic lattice is at room temperature. As a result of the strong nonequilibrium condition the excess of energy is transferred to the atomic lattice via electron-phonon coupling [8,9].

Instrumental to the investigation of the atomic dynamics following the energy transfer to the sample has been the development of tools capable of probing atomic details at the relevant timescales, which are of the order of picoseconds. Among these, x-ray free-electron lasers (XFELs) [10–14] are unique instruments to characterize structure and dynamics of condensed matter due to their exceptional properties in terms of brightness, temporal pulse duration and transverse coherence [15–17].

Several of the investigations cited above focused on gold. Differing by only one electron there is platinum, a noble metal with numerous scientific and technological applications. It is used, for example, for medical devices [18], in nanomedicine [19] and has a central role in cancer chemotherapy [20,21]. It is essential for the catalysis of the hydrogen oxidation and oxygen reduction reactions, at the core of fuel cells and electrolysers [22–24]. Due to its excellent performance and thermal stability, platinum is also extensively employed within automotive catalytic converters [25,26], and to catalyse several other industrially-relevant reactions, for example, in the oil industry [27]. The elevated chemical inertness, oxidation resistance, melting temperature, and phase stability of platinum [28] make it perfect to produce melting equipment. For example, it is used to manufacture glass fibers, for temperature sensors or for space industry applications [29]. Because of its properties, platinum is also used as reference for several applications, ranging from electrodes and thermometers to pressure calibrants [30].

In this work, we investigated the nonequilibrium melting of platinum induced by an ultrashort IR laser. In particular, we resolved the evolution of the atomic lattice and the appearance of the liquid phase in a time-resolved fashion by exploiting x rays produced by an XFEL. With our experiment and its interpretation, we aim at increasing the understanding of platinum properties, and in particular of the nucleation and propagation of the solid-liquid phase transition in

*Contact author: luca.gelisio@desy.de

†Present address: European XFEL, Holzkoppel 4, 22869 Schenefeld, Germany.

‡Present address: Beamline Division, Pohang Accelerator Laboratory, POSTECH, Pohang 37673, Republic of Korea.

§Contact author: ivan.vartaniants@desy.de

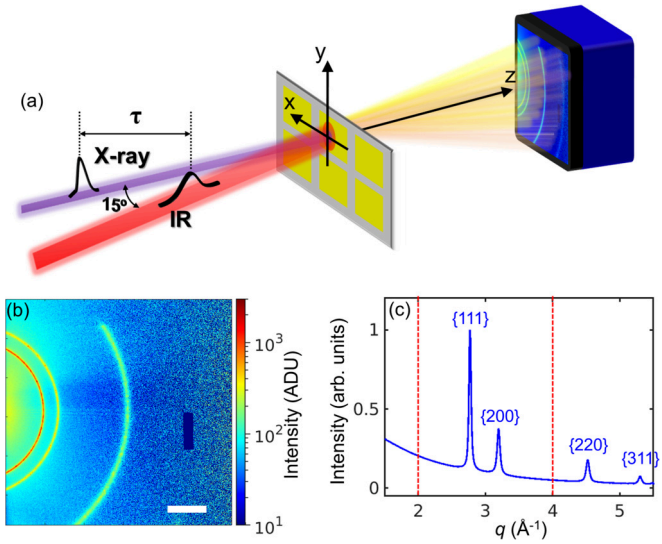

FIG. 1. (a) Schematic of the experimental setup. The IR laser impinges on the sample 15 degrees apart from the x-ray beam (perpendicular to the sample) on the horizontal plane. The silicon frame is moved in the *xy* plane before each shot to illuminate a different window. The x-ray scattering signal is measured on a pixelized detector positioned 108 mm downstream from the interaction region. (b) Typical x-ray single-pulse scattering pattern of a platinum reference sample (that is, the one without IR pump laser). The scale bar corresponds to 500 pixels in detector units. (c) Azimuthal average of the pattern in (b) as a function of momentum transfer where Bragg peaks from the face-centered cubic platinum {111}, {200}, {220}, and {311} family of planes can be observed. Vertical dashed lines indicate the region that is used for further analysis of the experimental data.

nanostructured thin films. Furthermore, the presented results are potentially of technological relevance, given the increasing demand of ultrafast laser manufacturing [31–36].

II. EXPERIMENT

Platinum films of 100 nm thickness were grown on silicon nitride membranes by electron beam evaporation. The resulting lateral dimension of the grains was of the order of 10 nm and they were preferentially columnar with respect to the film surface (see Ref. [37] for details). The experiment was performed at the Nano-crystallography and Coherent Imaging instrument (NCI) of the Pohang Accelerator Laboratory X-ray Free-Electron Laser (PAL-XFEL) [12,38]. A schematic of the experiment setup is shown in Fig. 1(a).

The x-ray beam propagating perpendicular to the sample surface was focused using a Kirkpatrick-Baez mirror system [39] on an area of approximately 5 μm in diameter on the sample (a representative imprint is shown in Fig. S4c [37]). The average x-ray photon energy during the experiment, measured by an on-line spectrometer, was 9.7 keV (see Sec. SII [37]). The resolution of the on-line spectrometer was estimated to be 0.26 eV full width at half maximum (FWHM) [40]. It should be noted that, due to the small thickness of the platinum samples the absorption of x rays is negligible (the attenuation length of platinum is 3.9 μm at the photon energy

TABLE I. IR fluences (Φ) and corresponding pulse energies ($\mathcal{E}$, measured using a laser power meter). The estimated energy densities absorbed by the sample ε are also reported.

Φ, mJ cm^{-2}	$\mathcal{E}$, μJ	ε, kJ/kg
100	28.4	139
200	57.0	279
300	85.0	416
400	113.0	553
500	141.0	691
1000	283.0	1386

employed during the experiment). Therefore, the scattering probability of x-ray photons at different sample depths was similar. Scattering data were collected on a Rayonix MX225-HS detector (2880×2880 pixels of size 78×78 μm^2 with a 2×2 binning mode). The detector was positioned downstream of the interaction region at a distance of 108 mm and its center was shifted from the x-ray axis by −37 and 1 mm along the *x* and *y* axes, respectively [the reference frame is shown in Fig. 1(a)]. The sample-detector distance was determined by fitting platinum Bragg peaks of the reference sample and assuming face-centered cubic (fcc) atomic arrangement with lattice constant $a_0 = 3.9236$ Å [41]. A typical single-pulse scattering pattern measured by the detector is shown in Fig. 1(b). Before each shot, the sample was moved in the plane perpendicular to the x-ray beam [the *xy* plane in Fig. 1(a)] so as to illuminate a different window (the sample geometry is detailed in Ref. [37]). Furthermore, the sample position along the x-ray beam (*z* axis) was adjusted in order to optimize the focal plane as seen by an inline microscope.

A Ti:sapphire laser of 800 nm central wavelength [42] and generating 100 fs (FWHM) pulses focused on an area of about 110 μm (FWHM) (see Sec. SIII [37]), was used to deposit energy into the samples. Its axis was 15° from the sample normal on the horizontal plane [see Fig. 1(a)]. The values of IR laser fluences, reported in Table I, were varied from 100 to 1000 mJ cm^{-2}. The time-delay between the IR pump and x-ray probe was varied from 1 ps to 1000 ps with logarithmic sampling. At least 10 patterns were collected for each combination of fluence and time delay. Given some uncertainty on the focal plane position and a drift of time zero across the experiment of about 0.5 ps, the error in time delay was estimated to be of the order of 1 ps (a detailed discussion on uncertainties associated to experimental results is given in Sec. SVIII [37]).

III. DATA ANALYSIS

The first step of the analysis of scattering data was the removal of the pedestal (dark signal) and so-called bad pixels. Each frame was further corrected by normalizing data by solid angle, x-ray polarization, linear absorption of x rays by the sample, and air scattering in the sample-detector path (see Sec. SIV for details [37]). Some regions of the detector were masked because the sample holder was partially blocking scattered intensity (see, for example, Fig. 1(b) and Fig. S8 [37]). A few detector frames (less than 7% of the total) were considered as outliers and discarded, for example, when the

x-ray beam was too close to an edge of the silicon frame. The average and standard deviation of the radial profile of each image were finally computed using the wavelength deduced from the in-line spectrometer. The momentum transfer axis (q) was binned with a bin size of 0.005 Å^{-1}. A typical radial profile for the reference sample, obtained by applying the above-mentioned pipeline to the detector images in Fig. 1(b), is shown in Fig. 1(c). High-q data were typically noisy and therefore the momentum range for further analysis was restricted to the interval from 2 to 4 Å^{-1} [see Fig. 1(c)]. In this region, face-centered cubic (fcc) platinum has two Bragg reflections, the ones associated to the {111} ($q = 2.774$ Å^{-1}) and {200} ($q = 3.203$ Å^{-1}) family of planes. To account for the contribution of scattering of x rays by air in the optical path and by the silicon nitride substrate, a membrane (no sample) was measured and fitted with a fourth order Chebyshev polynomial of the first kind. The result of the fit, $\mathcal{B}_0$, was then used to construct a general background function $\mathcal{B}(q) = \alpha\mathcal{B}_0\exp(\kappa q)$.

To fit the scattering curves we defined the following model as the sum of three contributions: (i) the background $\mathcal{B}(q)$ (two free parameters: α and κ), (ii) a pseudo-Voigt function for each Bragg peak (four free parameters: central position, FWHM, area of the curve, and the Lorentzian fraction), and (iii) the model proposed by Ashcroft and Lekner (AL) [43,44] for the liquid-like signal (three free parameters). Ashcroft and Lekner derived the liquid structure factor of a system of hard-spheres as a function of their diameter and packing density. As such, the model is simple and robust, and ideal for data whose quality is not particularly high (e.g., in terms of signal-to-noise ratio and extension of the momentum transfer range), like those collected in our experiment. Furthermore, the model proved to be successful in the interpretation of scattering data from various liquid metals (see, e.g., Refs. [43,45,46]). We additionally multiplied the structure factor described by the model by Ashcroft and Lekner by a scaling parameter and by the squared modulus of the platinum atomic form factor (coefficients were obtained from Ref. [47]). Further details on the fitting procedure are provided in Sec. SV [37].

IV. RESULTS AND DISCUSSION

The scattering curves collected during this experiment minus the background are shown in Fig. 2 for the different IR fluences used in this experiment. By visual inspection, at the lowest IR fluence of 100 mJ cm^{-2} no significant differences in the scattering data are observed at different time delays. However, starting from the IR fluence of 200 mJ cm^{-2}, we observe a gradual decrease of Bragg peak intensities with the increase of time delay. While at this IR fluence both the (111) and (200) Bragg peaks are visible for all time delays, already at 300 mJ cm^{-2} the higher-q peak (200) starts to disappear at about 100 ps. In general, the decrease of intensities is faster the higher the IR fluence. For example, at the fluence of 1000 mJ cm^{-2} Bragg peaks are practically vanishing after a few picoseconds from the IR pulse. At the same time, we would like to note here that some intensity corresponding to the (111) Bragg peak is observed for every fluence and time delay, indicating that some residual solid fraction is always present in the region of the sample probed by x rays. We

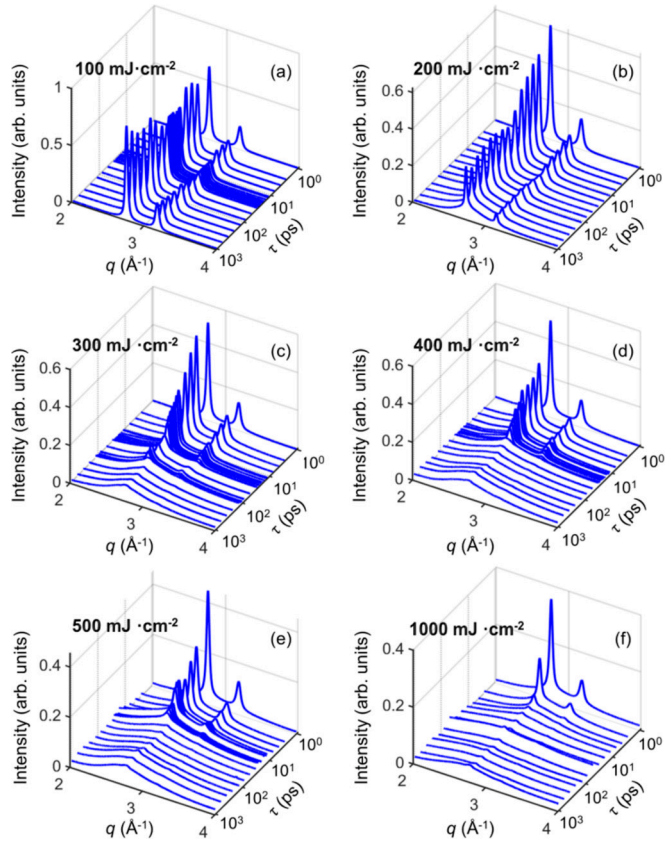

FIG. 2. Scattering curves at different time delays of the x-ray probe with respect to the IR pump for each IR fluence reported in Table I. The data sets are normalized by the average maximum intensity of the reference sample, which is collected in absence of IR radiation.

interpret the continuous scattering curve which appears as the intensity of Bragg peaks decreases as the fingerprint of the platinum liquid phase. By that, we conclude that platinum films are partially melted for fluences of 200 mJ cm^{-2} and higher. Below, a detailed analysis of the results obtained is presented.

The parameters extracted from the fit of scattering curves are reported in Fig. 3 as a function of pump-probe time delays. Each point in this figure is the median of the corresponding dataset (Fig. S11 exemplifies the scattering of individual values around the median [37]). Even if both the (111) and (200) Bragg peaks are present in the investigated momentum-transfer range, we restrict our analysis to the former, since the two are highly correlated within the resolution of our measurements (the analysis of the (200) Bragg peak is reported in Fig. S12 [37]).

The integrated intensity of the (111) Bragg peak, which is proportional to the amount of crystalline ordered fcc platinum in the probed region of the sample, is shown in Fig. 3(a). As it can be observed, for each value of the incident IR fluence this quantity is reduced with respect to the reference value (that is, measured without illuminating the sample with IR radiation). As discussed above, the decrease of integrated intensity within the investigated temporal range is negligible when the IR fluence equals to 100 mJ cm^{-2}, and modest when

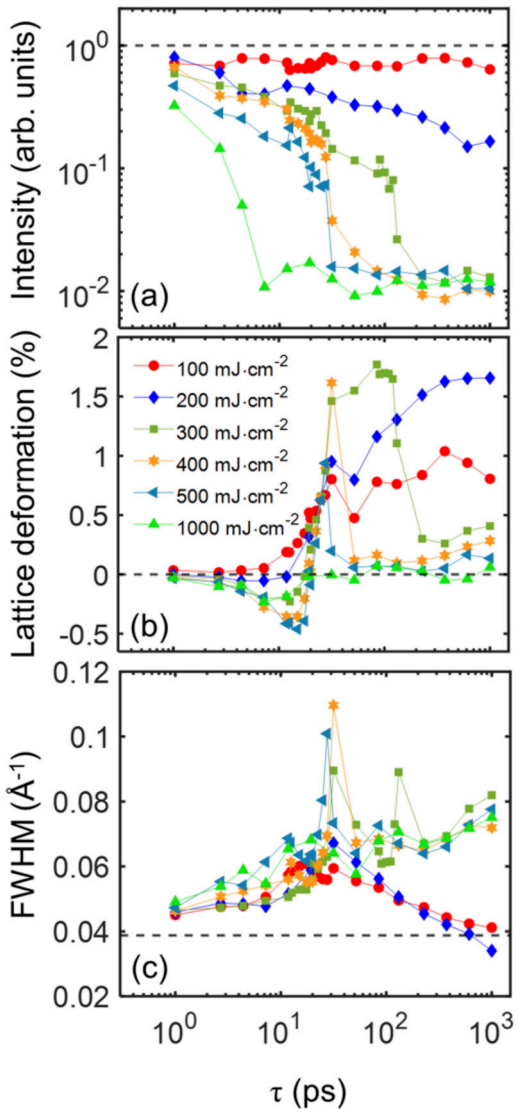

FIG. 3. Parameters deduced from the fitting of the (111) Bragg peak. (a) Integrated intensity normalized to its reference value, collected in absence of IR radiation, (b) lattice deformation (see text for details), and (c) FWHM. In all panels, the dashed lines correspond to reference values. Data is plotted as a function of the time delay between the IR pump and x-ray probe.

it is 200 mJ cm^{-2} (these will be named "low fluences"). On the contrary, for higher values ("high fluences") the integrated intensity drops to about 1% of the reference value, and the decay is faster the higher the fluence. This occurs from about one hundred picoseconds for 300 mJ cm^{-2} to a few picoseconds for 1000 mJ cm^{-2}.

The position of a Bragg peak q_{hkl} is related to the lattice parameter a of a cubic lattice through the known relation $a = 2\pi\sqrt{h^2+k^2+l^2}/q_{hkl}$. Variations of the time delay dependent strain $\varepsilon(\tau) = a(\tau)/a_0 - 1$, where a_0 and $a(\tau)$ are the lattice parameters for the reference structure and at time delay τ, are shown in Fig. 3(b). As it can be observed, for low fluences the lattice is expanded for each time delay longer than approximately 10 ps. This is compatible with an increase of the sample temperature. Assuming the expansion to be purely thermal, the temperature can be evaluated from the equation $a = \alpha_T(T - T_0)$, where α_T is the thermal expansion coefficient [48] and $T_0 = 300$ K. The maximum temperature at the longest measured time delay (one nanosecond) was estimated to be about 1300 K and 1800 K for IR fluences of 100 and 200 mJ cm^{-2}, respectively.

The general trend for each IR fluence greater than 100 mJ cm^{-2} is that the lattice is progressively more compressed in the first 10–20 ps, with a strain rate of the order of 10^8 s^{-1} and up to approximately $\varepsilon = -0.5\%$ at the IR fluence of 500 mJ cm^{-2}. The compression value is increasing with IR fluence, except for 1000 mJ cm^{-2}, likely due to the extremely small residual solid state fraction [see Fig. 3(a)]. After the maximum value of compression is reached, the lattice rapidly expands for every fluence (strain rate $\sim 10^9$ s^{-1}) up to time delays of approximately 30 ps. This is about the time necessary for a sound wave to transverse the thickness of the platinum sample, which is 31 ps assuming the (longitudinal) speed of sound of 3260 m/s [49], and enough for the electron-ion temperature gradient to vanish (see Fig. S15 [37]). We attribute the negative atomic displacement to the pressure resulting from the inhomogeneous distribution of ion temperatures in the platinum sample. In fact, the energy deposited by the IR source is strongly localized in a thin layer during the first picoseconds after the IR pulse (see Sec. SVII [37]), also owing to the abundance of grain boundaries limiting electron motion in our samples (see Sec. SI [37]). We speculate that the expansion of this layer compresses the rest of the sample. This picture is consistent with the one in Ref. [6]. After the displacement wave has traveled the film at the speed of sound, for low fluences the strain values decrease slightly up to time delays of about ~50–60 ps (approximately the time needed for the sound wave to travel back to the surface), to then increase again. For high fluences, in general, the expansion diminishes, following the same trend already observed for the residual fcc solid state fraction [see Fig. 3(a)].

The FWHM of the (111) Bragg reflection is shown in Fig. 3(c). It is inversely proportional to the size of the coherently scattering domains and proportional to the microstrain and thermal vibrations in the sample [50]. For each value of the IR fluence, the peak width is initially slightly increased with respect to the reference value. At about 30 ps, we observe a rapid increase of the peak width, possibly indicating inhomogeneous distribution of strain in the sample, followed by a fast decay. The curve has a maximum at the time point 31.6 ps for fluences lower than 500 mJ cm^{-2}, which is anticipated by a few picoseconds for the latter. This is likely due to extremely small residual fcc fraction at this time delay [see Fig. 3(a)], which might also explain why the peak width for the IR fluence of 1000 mJ cm^{-2} does not follow a similar trend. It is interesting to note, that for low fluences, the FWHM at 1 ns is practically returning to the reference value. In particular, for the 200 mJ cm^{-2} case the final FWHM value in the sub-nanosecond time delay region is even lower than the reference one, possibly indicating an increase of the crystallite size due to sintering of smaller grains or relaxation of residual stresses. Contrarily, for high fluences, the values of FWHM after the peak at 31.6 ps continue to increase.

The Kirchhoff's law predicts, for a constant pressure process, the change of the temperature T of the system as a

function of enthalpy $\mathcal{H}$ to be $dT = d\mathcal{H}/c_p(T)$. Assuming that the energy absorbed by the system (see Table I) is solely increasing its temperature, the above equation estimates a maximum temperature of ∼1300 K for IR fluence of 100 mJ cm^{-2}. This is lower than the melting temperature for platinum at atmospheric pressure, $T_M = 2041.3$ K [51], and therefore the sample should remain solid. It should be noted that this is the same temperature estimated from the position of the (111) Bragg peak, and that no evidence of scattering from liquid phase is detected in our analysis. For the IR fluence of 200 mJ cm^{-2} the melting should be partial, with coexistence of the solid and liquid phases, whereas 300 mJ cm^{-2} should be sufficient to transform the entire solid sample into liquid. This picture is apparently consistent with Fig. 3(a) for long time delays although an extremely small residual fcc solid state fraction is always present according to our experimental findings. We speculate that this might be due to chemical stabilization of platinum at its interface with the Si_3N_4 film, inhibiting solid-to-liquid phase transition.

The scattering curve attributed to liquid, which is clearly distinguishable from the Bragg peaks, was fitted using the AL model. It should be noted that, especially for low fluences and short pump-probe delays, this model is likely to fit the diffuse scattering due to various defects including thermal vibrations, and might therefore not provide correct information on the liquid phase. The area under the AL curve, which is proportional to the amount of liquid phase, was estimated by integrating the corresponding analytical model from the origin of momentum-transfer space to infinity. To compensate for fluctuations of the incoming x-ray intensities, we divided the integral by the total intensity in the background for each diffraction pattern. The result is shown in Fig. 4(a). Here, no data are shown for the IR fluence of 100 mJ cm^{-2} and early time delays for 200 and 300 mJ cm^{-2} as no liquid is detected in our analysis for these fluences. The general trend is that the integral of the liquid curve increases as a function of the time delay, indicating development of the liquid fraction. It also increases in magnitude as a function of the IR fluence, although there is no significant difference between 400 and 500 mJ cm^{-2}. Moreover, at time delays of hundreds of picoseconds the values of integrated intensities for the IR fluence of 1000 mJ cm^{-2} are similar to the ones for 200 mJ cm^{-2}. This is compatible with the trend of integrated intensities of the (111) Bragg reflection discussed in relation to Fig. 3(a). To explain this we evaluated the conditions for ablation using the approach described in Ref. [52] (see Sec. SVI [37]). According to this, the estimated crater depth is about 1 and 10 nm for the IR fluences of 500 and 1000 mJ cm^{-2}, respectively (see Sec. SVI for the details of ablation estimate [37]), which justifies the deviation of integrated intensities trends for the highest fluence.

In the AL model [43,44], the profile of the scattering curve of a liquid of hard spheres is defined by their diameter d and packing density η. The two parameters are in turn related to the liquid density of platinum ρ by the relation $\rho = 6\pi\eta A_{Pt}/d^3$, where $A_{Pt} = 195.08$ g/mol is the atomic weight of platinum. The density of the liquid phase, shown in Fig. 4(b), does not show a clear trend for time delays shorter than about 10 ps. However, if we exclude the data for 200 and 300 mJ cm^{-2}, both associated with a small liquid fraction

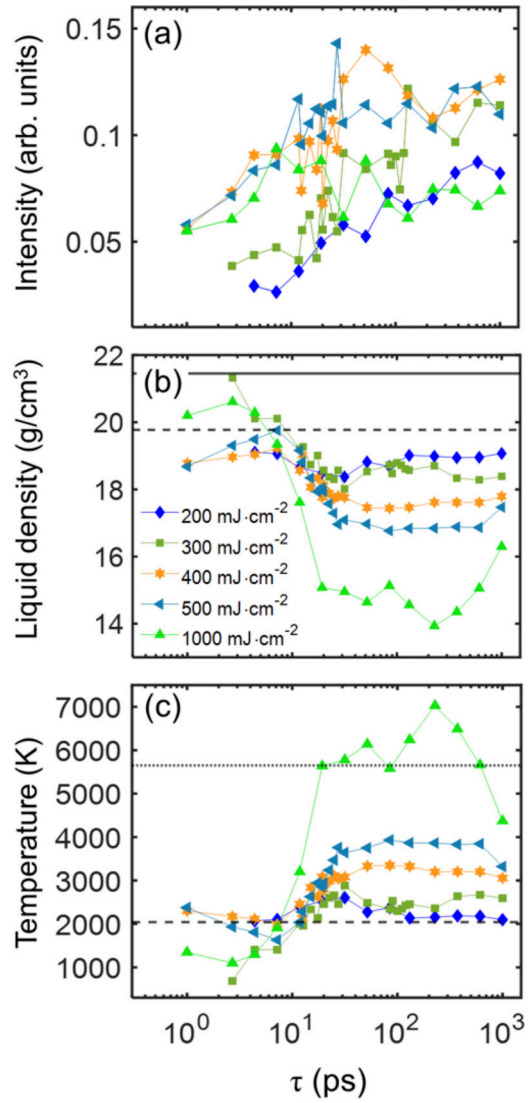

FIG. 4. Quantities extracted from the liquid phase model (see text for details). (a) Integrated intensity normalized to the background intensity, (b) liquid density, and (c) temperature. In (b), the dashed and solid lines indicate the nominal values for the liquid and solid density, respectively, and in (c), dashed and dotted lines indicate the melting and boiling temperatures, respectively. Data are plotted as a function of the time delay between the IR pump and x-ray probe. We excluded the lowest fluence of 100 mJ cm^{-2} at which no liquid phase was detected.

[see Fig. 4(a)], then the higher the fluence the denser is the liquid. We speculate that this might be due to the residual solid fraction [see Fig. 3(a)], mechanically constraining the liquid phase. On the contrary, for time delays larger than approximately 30 ps, the liquid density is lower than the reference value at the melting point [53], 19.77 g cm^{-3}. It is also lower the higher is the IR fluence, which is compatible with an increase of the liquid temperature. The transition between the two density states is roughly larger in magnitude and faster in time the higher is the IR fluence. Interestingly, the temporal region between approximately 10 and 30 ps corresponds to both a transition between two different states of density, and of strain in the lattice [see Fig. 3(b)], suggesting that the solid and

liquid phase might experience the same mechanical pressure. When the compressive strain is relieved, the density of the liquid decreases (its volume increases).

The temperature of the liquid phase can be estimated from Ref. [54] as $T = (V/V_0 - 0.89125)/8.3955 \times 10^{-5}$, where the volume V is calculated from the density as obtained from the AL model, and $V_0 = 4.673 \times 10^{-5}$ m^3 kg^{-1}. It should be noted that this equation is valid in the interval of temperatures from 2042 to 5650 K, and it assumes a constant pressure process. Values of temperature of the liquid phase, shown in Fig. 4(c), outside this range are in general the ones corresponding to time delays shorter than 10 ps, or to the highest IR fluence of 1000 mJ cm^{-2}. The values within the range of validity of the equation, in Fig. 4(c), confirm that the temperature of the liquid phase increases with the IR fluence. In particular, the temperature approximately equals the melting one, at which solid and liquid coexist, for the IR fluence of 200 mJ cm^{-2}, and it reaches almost 4000 K for 500 mJ cm^{-2}.

To support the interpretation of experimental results, we performed simulations exploiting the two-temperature model (TTM) [55] (see for details Sec. SVII [37]). The TTM is a phenomenological description of the spatiotemporal evolution of the temperature in a metal following its ultrafast excitation. In this picture, the laser pulse is absorbed by free electrons near the surface and increases their energy. This is then partially transferred to the lattice via electron-phonon coupling at longer timescales. The TTM assumes a continuous media and does not include any defects, like the grain boundaries, present in the investigated samples which diminish the amount of energy required for the solid-liquid phase transition (heterogeneous melting) [5].

In Fig. 5, we compare the fraction of fcc solid estimated from the experimental data and the one obtained from the TTM model. The values of experimental data are calculated assuming that the integral of the (111) Bragg peak is proportional to the amount of solid phase, and that there is no liquid platinum at the time delay of 1 ps. The value of the peak integral at this time delay is, therefore, used to normalize all the other values. For the case of the TTM simulations, the fraction of solid is simply the thickness of the solid phase at a given time from the IR pulse divided by the total thickness of the simulation domain, which is 100 nm in our case (details on the assessment of the liquid fraction are provided in Sec. SVII [37]). All simulation parameters, including the electron-phonon coupling parameter G_{ep}, which rules the energy exchange between the electronic and ionic subsystems, were taken from the known references (see Sec. SVII for details [37]). As it can be observed from Fig. 5, the model qualitatively captures the trends observed experimentally. For the IR fluence of 100 mJ cm^{-2} it does not predict any formation of the liquid phase, which is compatible to our experimental findings. From the fluence of 200 mJ cm^{-2}, the liquid phase is formed starting from about a few picoseconds. The time delay for the nucleation of the liquid phase is becoming shorter with increasing the IR fluence [which seems to be consistent with Fig. 4(a)], ranging between approximately 2 and 4 ps for the highest and lowest IR fluence, respectively. It should be noted that for all fluences experimental results seem to indicate a faster nucleation of the liquid phase with respect to simulations. This could be explained both by

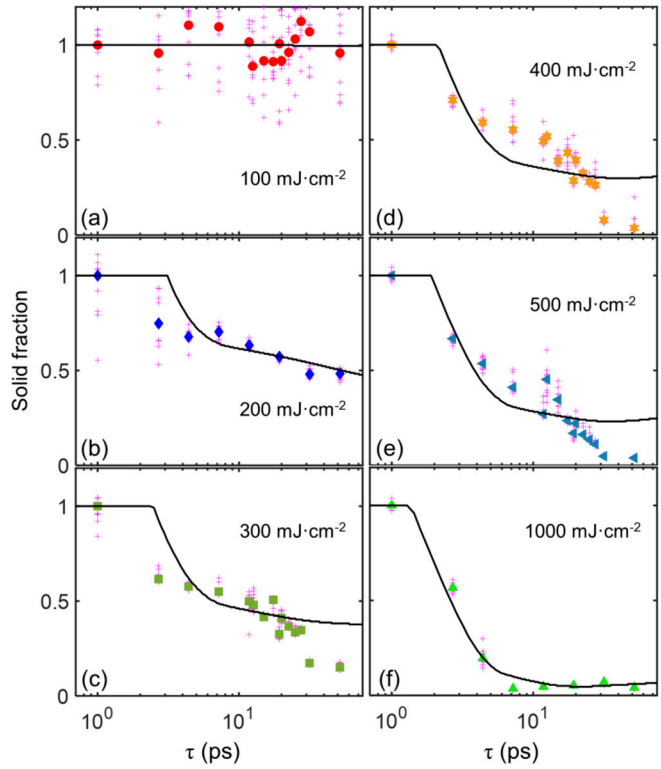

FIG. 5. Solid state fraction. Dots are the median values for a given time delay and pink crosses are the values calculated from the experimental data. The solid black line is calculated from the TTM simulations.

inaccurate simulation parameters, or the heterogeneous nature of melting. In fact, our samples contain a considerable amount of defects, and especially of grain boundaries (see Fig. S2 [37]). These can act as nucleation seeds for the solid-liquid phase transition, which therefore requires less energy with respect to a defect-free sample. It is worth pointing out that our TTM simulation does not include any structural defects, and therefore models homogeneous melting. When simulation parameters are concerned, the electron-phonon coupling and the electron ballistic range play a particularly critical role in defining the temporal evolution of the atomic lattice, and in particular in defining the equilibration time. For example, our simulations show that increasing/reducing the magnitude of the electron-phonon coupling parameter by a factor of two is reducing/increasing the equilibration time of temperatures of electrons and ions by about 10 ps (see Fig. S16 [37]). For IR fluences from 300 mJ cm^{-2} to 500 mJ cm^{-2} we observe a second drop of the solid fraction derived from experimental data at about 20–30 ps, which is not explained by the TTM simulations. For these fluences, this is about the time delay corresponding to a considerable decrease of integrated intensities [Fig. 3(a)], dissipation of the compression field [Fig. 3(b)], and maximization of the crystal disorder [Fig. 3(c)]. Furthermore, in the same temporal region the density of the liquid (and in turn, its temperature) changes considerably in magnitude [Fig. 4(b)]. We speculate that the dissipation of the compression field destabilizes the lattice promoting the creation of additional liquid phase. This should be supported

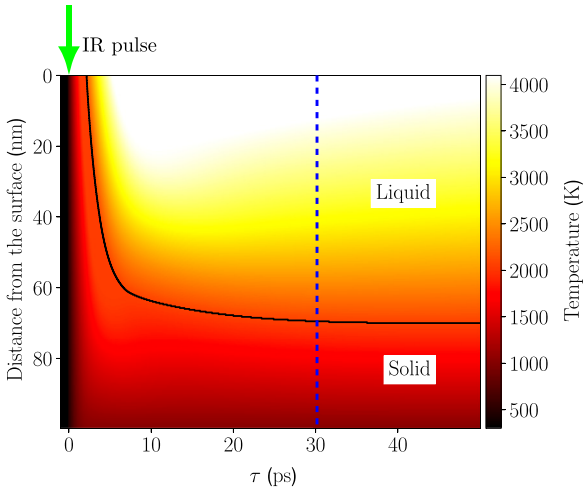

FIG. 6. Schematic of experimental facts as a function of distance from the surface of the sample and time delay τ, for the IR fluence of 400 mJ cm^{-2}. The temperature of ions as predicted by our TTM simulations is shown together with the different sample phases (solid and liquid), separated by a black curve. The solid state fraction is compared to experimental data in Fig. 5. The blue dashed line marks the time needed for a sound wave originated at the surface of the sample and traveling at the speed of sound to reach the bottom of the sample, 100 nm from the surface. We speculate that this is a compression wave whose fingerprint in term of lattice displacement can be observed in Figs. 3(b) and 3(c). After this point in time, the lattice deformation is positive. The compression field is attributed to the strong temperature gradient established in the first picoseconds and nanometers. We speculate that the same gradient is responsible for the drop of scattered intensities [see Fig. 3(a)], the atomic displacement observed in the sample [see Fig. 3(b)], and its inhomogeneous distribution, which in turn can explain the trend of the width of the (111) Bragg peaks [see Fig. 3(c)].

by the integrated intensity of the liquid phase, shown in Fig. 4(a). However, while for the IR fluence of 400 mJ cm^{-2} a considerable increase of this quantity can be observed from approximately 20 ps, this is not the case for other fluences, which might be due to the measurement uncertainty. Finally, it is worth mention the excellent agreement between the solid fraction calculated from experimental data and TTM simulations for the highest IR fluence of 1000 mJ cm^{-2}, although, we recall, the sample is partially ablated in this case.

We summarized the main findings presented in this manuscript in Fig. 6.

V. SUMMARY AND OUTLOOK

In summary, here we described the evolution of platinum nanostructured films illuminated by ultrashort IR radiation at several fluences and time delays. We observed a thermal strain wave traveling perpendicular to the film at the speed of sound. The sample remained completely solid when the fluence was 100 mJ cm^{-2}, and it was partially liquid for higher fluences, with the liquid phase developing at time delays of a few picoseconds. We observed that lattice deformations before the sound wave traveled through the entire sample were mostly compressive, and expansive after that. Furthermore, analysis of our experimental results employing the AL's model suggested that the density of the liquid phase was changing considerably after the sound wave propagated through the sample.

To support experimental findings, we performed TTM simulations, which predicted the sample to be solid at the IR fluence of 100 mJ cm^{-2}, and partially liquid for higher fluences, with the solid fraction decreasing the more the higher the fluence. We furthermore observed an additional drop of the solid fraction which is not described by TTM simulations at fluences from 300 to 500 mJ cm^{-2}, and time delays longer than 30 ps. We speculated that this might be due to the release of the compressive field, which destabilizes the lattice and promotes the nucleation of the liquid phase.

Overall, our TTM simulations, based on a model of a uniform sample, does not seem to be sufficient to capture the complexity of the solid-liquid phase transition in polycrystalline films illuminated by femtosecond IR light. In particular, the ablation process or the presence of defects such as grain boundaries are not taken into account in the TTM simulations.

Finally, we believe that a deeper understanding of the results presented here requires more extensive experimental and theoretical exploration in the future, for example, exploiting TTM simulations coupled to molecular dynamics [56,57]. We also think that research performed at XFEL facilities will be instrumental in answering the questions outlined in this work.

ACKNOWLEDGMENTS

The use of the computing power of the Korea supercomputer center to transfer data from PAL XFEL to the DESY storage system and the Maxwell computational resources operated at Deutsches Elektronen-Synchrotron (DESY) is acknowledged. The authors would like to thank S. Lazarev for the stimulating discussions while planning the experiment. The authors acknowledge fruitful discussions with M. Altarelli and I. K. Robinson, and careful reading of the manuscript by H.-P. Liermann and G. Hinsley. The authors would like to thank referees for their constructive criticism. L.G., Y.Y.K., R.K., and I.A.V. acknowledge the support by the Helmholtz Associations Initiative and Networking Fund (Grant No. HRSF-0002). D.N. was supported by the National Research Foundation of Korea (Grants No. 2021R1F1A1051444 and No. 2022M3H4A1A04074153). S.W.L. and C.U.K. acknowledge the support by the National Research Foundation of Korea (NRF) grant funded by the Korea government (NRF-2022R1A2C2091815). The experiments were carried out using the CXI instrument at PAL-XFEL (Proposal No. 2019-1st-NCI-016) funded by the Ministry of Science and ICT of Korea. This work was supported by the Global Science Experimental Data Hub Center (GSDC) for data computing and the Korea Research Environment Open NETwork (KREONET) for network service provided by the Korea Institute of Science and Technology Information (KISTI).

[1] S. Williamson, G. Mourou, and J. C. M. Li, Time-resolved laser-induced phase transformation in aluminum, Phys. Rev. Lett. **52**, 2364 (1984).

[2] B. J. Siwick, J. R. Dwyer, R. E. Jordan, and R. J. D. Miller, An atomic-level view of melting using femtosecond electron diffraction, Science **302**, 1382 (2003).

[3] R. Ernstorfer, M. Harb, C. T. Hebeisen, G. Sciaini, T. Dartigalongue, and R. J. D. Miller, The formation of warm dense matter: Experimental evidence for electronic bond hardening in gold, Science **323**, 1033 (2009).

[4] M. Z. Mo, Z. Chen, R. K. Li, M. Dunning, B. B. L. Witte, J. K. Baldwin, L. B. Fletcher, J. B. Kim, A. Ng, R. Redmer, A. H. Reid, P. Shekhar, X. Z. Shen, M. Shen, K. Sokolowski-Tinten, Y. Y. Tsui, Y. Q. Wang, Q. Zheng, X. J. Wang, and S. H. Glenzer, Heterogeneous to homogeneous melting transition visualized with ultrafast electron diffraction, Science **360**, 1451 (2018).

[5] T. A. Assefa, Y. Cao, S. Banerjee, S. Kim, D. Kim, H. Lee, S. Kim, J. H. Lee, S.-Y. Park, I. Eom, J. Park, D. Nam, S. Kim, S. H. Chun, H. Hyun, K. S. Kim, P. Juhas, E. S. Bozin, M. Lu, C. Song *et al.*, Ultrafast x-ray diffraction study of melt-front dynamics in polycrystalline thin films, Sci. Adv. **6**, eaax2445 (2020).

[6] A. F. Suzana, R. Koch, L. Wu, T. A. Assefa, S. Kim, S. Choi, H. Lee, S. Kim, J. H. Lee, S.-Y. Park, D. Nam, S. Kim, H. Hyun, K. S. Kim, G. Wright, E. S. Bozin, C. Song, H. Kim, S. J. L. Billinge, and I. K. Robinson, Compressive effects in melting of palladium thin films studied by ultrafast x-ray diffraction, Phys. Rev. B **107**, 214303 (2023).

[7] I. K. Robinson, J. P. Griffiths, R. Koch, T. A. Assefa, A. F. Suzana, Y. Cao, S. Kim, D. Kim, H. Lee, S. Kim, J. H. Lee, S.-Y. Park, I. Eom, J. Park, D. Nam, S. Kim, S. H. Chun, H. Hyun, K.-S. Kim, M. Lu *et al.*, Emergence of liquid following laser melting of gold thin films, IUCrJ **10**, 656 (2023).

[8] S. I. Anisimov and B. Rethfeld, Theory of ultrashort laser pulse interaction with a metal, in *Nonresonant Laser-Matter Interaction (NLMI-9)*, edited by V. I. Konov and M. N. Libenson (SPIE, 1997), Vol. 3093, p. 192.

[9] E. Gamaly, *Femtosecond Laser-Matter Interactions: Theory, Experiments and Applications* (Pan Stanford Publishing Pte Ltd, Singapore, 2011).

[10] P. Emma, R. Akre, J. Arthur, R. Bionta, C. Bostedt, J. Bozek, A. Brachmann, P. Bucksbaum, R. Coffee, F.-J. Decker *et al.*, First lasing and operation of an ångstrom-wavelength free-electron laser, Nat. Photonics **4**, 641 (2010).

[11] T. Ishikawa, H. Aoyagi, T. Asaka, Y. Asano, N. Azumi, T. Bizen, H. Ego, K. Fukami, T. Fukui, Y. Furukawa *et al.*, A compact x-ray free-electron laser emitting in the sub-ångström region, Nat. Photonics **6**, 540 (2012).

[12] H.-S. Kang, C.-K. Min, H. Heo, C. Kim, H. Yang, G. Kim, I. Nam, S. Y. Baek, H.-J. Choi, G. Mun *et al.*, Hard x-ray free-electron laser with femtosecond-scale timing jitter, Nat. Photonics **11**, 708 (2017).

[13] W. Decking, S. Abeghyan, P. Abramian, A. Abramsky, A. Aguirre, C. Albrecht, P. Alou, M. Altarelli, P. Altmann, K. Amyan *et al.*, A MHz-repetition-rate hard X-ray free-electron laser driven by a superconducting linear accelerator, Nat. Photonics **14**, 391 (2020).

[14] E. Prat, R. Abela, M. Aiba, A. Alarcon, J. Alex, Y. Arbelo, C. Arrell, V. Arsov, C. Bacellar, C. Beard *et al.*, A compact and cost-effective hard X-ray free-electron laser driven by a high-brightness and low-energy electron beam, Nat. Photonics **14**, 748 (2020).

[15] I. A. Vartanyants, A. Singer, A. P. Mancuso, O. M. Yefanov, A. Sakdinawat, Y. Liu, E. Bang, G. J. Williams, G. Cadenazzi, B. Abbey, H. Sinn, D. Attwood, K. A. Nugent, E. Weckert, T. Wang, D. Zhu, B. Wu, C. Graves, A. Scherz, J. J. Turner *et al.*, Coherence properties of individual femtosecond pulses of an X-Ray Free-Electron Laser, Phys. Rev. Lett. **107**, 144801 (2011).

[16] R. Khubbutdinov, N. Gerasimova, G. Mercurio, D. Assalauova, J. Carnis, L. Gelisio, L. Le Guyader, A. Ignatenko, Y. Y. Kim, B. E. Van Kuiken, R. P. Kurta, D. Lapkin, M. Teichmann, A. Yaroslavtsev, O. Gorobtsov, A. P. Menushenkov, M. Scholz, A. Scherz, and I. A. Vartanyants, High spatial coherence and short pulse duration revealed by the Hanbury Brown and Twiss interferometry at the European XFEL, Struct. Dyn. **8**, 044305 (2021).

[17] Y. Y. Kim, R. Khubbutdinov, J. Carnis, S. Kim, D. Nam, I. Nam, G. Kim, C. H. Shim, H. Yang, M. Cho, C.-K. Min, C. Kim, H.-S. Kang, and I. A. Vartanyants, Statistical analysis of hard X-ray radiation at the PAL-XFEL facility performed by Hanbury Brown and Twiss interferometry, J. Synchrotron Radiat. **29**, 1465 (2022).

[18] A. Cowley and B. Woodward, A healthy future: Platinum in medical applications, Platin. Met. Rev. **55**, 98 (2011).

[19] D. Pedone, M. Moglianetti, E. De Luca, G. Bardi, and P. P. Pompa, Platinum nanoparticles in nanobiomedicine, Chem. Soc. Rev. **46**, 4951 (2017).

[20] D. Wang and S. J. Lippard, Cellular processing of platinum anticancer drugs, Nat. Rev. Drug Discov. **4**, 307 (2005).

[21] L. Kelland, The resurgence of platinum-based cancer chemotherapy, Nat. Rev. Cancer **7**, 573 (2007).

[22] J. Wu and H. Yang, Platinum-based oxygen reduction electrocatalysts, Acc. Chem. Res. **46**, 1848 (2013).

[23] W. Sheng, Z. Zhuang, M. Gao, J. Zheng, J. G. Chen, and Y. Yan, Correlating hydrogen oxidation and evolution activity on platinum at different pH with measured hydrogen binding energy, Nat. Commun. **6**, 5848 (2015).

[24] J. Fan, M. Chen, Z. Zhao, Z. Zhang, S. Ye, S. Xu, H. Wang, and H. Li, Bridging the gap between highly active oxygen reduction reaction catalysts and effective catalyst layers for proton exchange membrane fuel cells, Nat. Energy **6**, 475 (2021).

[25] H. Sharma and A. Mhadeshwar, A detailed microkinetic model for diesel engine emissions oxidation on platinum based diesel oxidation catalysts (DOC), Appl. Catal. B **127**, 190 (2012).

[26] Y. Y. Kim, T. F. Keller, T. J. Goncalves, M. Abuin, H. Runge, L. Gelisio, J. Carnis, V. Vonk, P. N. Plessow, I. A. Vartaniants, and A. Stierle, Single alloy nanoparticle x-ray imaging during a catalytic reaction, Sci. Adv. **7**, eabh0757 (2021).

[27] A. E. Hughes, N. Haque, S. A. Northey, and S. Giddey, Platinum group metals: A review of resources, production and usage with a focus on catalysts, Resources **10**, 93 (2021).

[28] S. Anzellini, V. Monteseguro, E. Bandiello, A. Dewaele, L. Burakovsky, and D. Errandonea, In situ characterization of the high pressure –high temperature melting curve of platinum, Sci. Rep. **9**, 13034 (2019).

[29] B. Fischer, New platinum materials for high temperature applications, Adv. Eng. Mater. **3**, 811 (2001).

[30] D. E. Fratanduono, M. Millot, D. G. Braun, S. J. Ali, A. Fernandez-Pañella, C. T. Seagle, J.-P. Davis, J. L. Brown, Y.

Akahama, R. G. Kraus, M. C. Marshall, R. F. Smith, E. F. O'Bannon, J. M. McNaney, and J. H. Eggert, Establishing gold and platinum standards to 1 terapascal using shockless compression, Science **372**, 1063 (2021).

[31] M. Malinauskas, A. Žukauskas, S. Hasegawa, Y. Hayasaki, V. Mizeikis, R. Buividas, and S. Juodkazis, Ultrafast laser processing of materials: from science to industry, Light Sci. Appl. **5**, e16133 (2016).

[32] A. Y. Vorobyev and C. Guo, Direct femtosecond laser surface nano/microstructuring and its applications, Laser Photonics Rev. **7**, 385 (2013).

[33] A. Y. Vorobyev and C. Guo, Metal pumps liquid uphill, Appl. Phys. Lett. **94**, 224102 (2009).

[34] R. A. Green, P. B. Matteucci, C. W. D. Dodds, J. Palmer, W. F. Dueck, R. T. Hassarati, P. J. Byrnes-Preston, N. H. Lovell, and G. J. Suaning, Laser patterning of platinum electrodes for safe neurostimulation, J. Neural Eng. **11**, 056017 (2014).

[35] L. Li, C. Jiang, and L. Li, Hierarchical platinum–iridium neural electrodes structured by femtosecond laser for superwicking interface and superior charge storage capacity, Bio-Des. Manuf. **5**, 163 (2022).

[36] N. G. Semaltianos, Nanoparticles by laser ablation, Crit. Rev. Solid State Mater. Sci. **35**, 105 (2010).

[37] See Supplemental Material at http://link.aps.org/supplemental/10.1103/PhysRevB.110.144303 for details of platinum samples, x-ray spectrum, infrared laser, data anaysis, fitting of radial profiles, sample ablation due to IR light, two-temperature model simulations, and uncertainties of results, which also contains Refs. [58–81].

[38] J. Park, S. Kim, K.-H. Nam, B. Kim, and I. S. Ko, Current status of the CXI beamline at the PAL-XFEL, J. Korean Phys. Soc. **69**, 1089 (2016).

[39] P. Kirkpatrick and A. V. Baez, Formation of optical images by x rays, J. Opt. Soc. Am. **38**, 766 (1948).

[40] I. Nam, C.-K. Min, B. Oh, G. Kim, D. Na, Y. J. Suh, H. Yang, M. H. Cho, C. Kim, M.-J. Kim, C. H. Shim, J. H. Ko, H. Heo, J. Park, J. Kim, S. Park, G. Park, S. Kim, S. H. Chun, H. Hyun *et al.*, High-brightness self-seeded X-ray free-electron laser covering the 3.5 keV to 14.6 keV range, Nat. Photonics **15**, 435 (2021).

[41] J. W. Arblaster, Crystallographic properties of platinum, Platinum Metals Rev. **41**, 12 (1997).

[42] M. Kim, C.-K. Min, and I. Eom, Laser systems for time-resolved experiments at the Pohang Accelerator Laboratory X-ray Free-Electron Laser beamlines, J. Synchrotron Radiat. **26**, 868 (2019).

[43] N. W. Ashcroft and J. Lekner, Structure and resistivity of liquid metals, Phys. Rev. **145**, 83 (1966).

[44] J. S. Pedersen, Determination of size distribution from small-angle scattering data for systems with effective hard-sphere interactions, J. Appl. Crystallogr. **27**, 595 (1994).

[45] A. J. Greenfield, J. Wellendorf, and N. Wiser, X-ray determination of the static structure factor of liquid Na and K, Phys. Rev. A **4**, 1607 (1971).

[46] G. Shen, V. B. Prakapenka, M. L. Rivers, and S. R. Sutton, Structure of liquid iron at pressures up to 58 GPa, Phys. Rev. Lett. **92**, 185701 (2004).

[47] P. J. Brown, A. G. Fox, E. N. Maslen, M. A. O'Keefe, and B. T. M. Willis, Intensity of diffracted intensities, in *International Tables for Crystallography Volume C: Mathematical, Physical and Chemical Tables*, edited by E. Prince (Springer Netherlands, Dordrecht, 2006).

[48] R. K. Kirby, Platinum—a thermal expansion reference material, Int. J. Thermophys. **12**, 679 (1991).

[49] M. de Podesta, *Understanding the Properties of Matter*, 2nd ed. (Taylor and Francis, London, 2002).

[50] B. E. Warren, *X-Ray Diffraction* (Addison-Wesley Publishing Company, Boston, Massachusetts, USA, 1969).

[51] N. Bergeard, S. Schaffert, V. López-Flores, N. Jaouen, J. Geilhufe, C. M. Günther, M. Schneider, C. Graves, T. Wang, B. Wu, A. Scherz, C. Baumier, R. Delaunay, F. Fortuna, M. Tortarolo, B. Tudu, O. Krupin, M. P. Minitti, J. Robinson, W. F. Schlotter *et al.*, Irreversible transformation of ferromagnetic ordered stripe domains in single-shot infrared-pump/resonant-x-ray-scattering-probe experiments, Phys. Rev. B **91**, 054416 (2015).

[52] E. G. Gamaly, A. V. Rode, B. Luther-Davies, and V. T. Tikhonchuk, Ablation of solids by femtosecond lasers: Ablation mechanism and ablation thresholds for metals and dielectrics, Phys. Plasmas **9**, 949 (2002).

[53] S. Mehmood, U. E. Klotz, and G. Pottlacher, Thermophysical properties of platinum-copper alloys, Metall. Mater. Trans. A **43**, 5029 (2012).

[54] R. S. Hixson and M. A. Winkler, Thermophysical properties of liquid platinum, Int. J. Thermophys. **14**, 409 (1993).

[55] S. I. Anisimov, B. L. Kapeliovich, and T. Perel'man, Electron emission from metal surfaces exposed to ultrashort laser pulses, Zh. Eksp. Teor. Fiz. **66**, 776 (1974) [Sov. Phys. JETP **39**, 375 (1974)].

[56] D. M. Duffy and A. M. Rutherford, Including the effects of electronic stopping and electron–ion interactions in radiation damage simulations, J. Phys.: Condens. Matter **19**, 016207 (2006).

[57] A. M. Rutherford and D. M. Duffy, The effect of electron–ion interactions on radiation damage simulations, J. Phys.: Condens. Matter **19**, 496201 (2007).

[58] L. R. Feret, La grosseur des grains des matières pulvérulentes, Assoc. Internat. pour l'Essai des Mat. **2**, 428 (1930).

[59] T. Wagner, ij-particlesizer: ParticleSizer 1.0.1, Zenodo (2016), doi:10.5281/zenodo.56457.

[60] C. A. Schneider, W. S. Rasband, and K. W. Eliceiri, NIH Image to ImageJ: 25 years of image analysis, Nat. Methods **9**, 671 (2012).

[61] M. Newville, T. Stensitzki, D. B. Allen, and A. Ingargiola, LMFIT: Non-Linear Least-Square Minimization and Curve-Fitting for Python (2014), https://zenodo.org/records/11813.

[62] I. S. Ko, H.-S. Kang, H. Heo, C. Kim, G. Kim, C.-K. Min, H. Yang, S. Y. Baek, H.-J. Choi, G. Mun, B. R. Park, Y. J. Suh, D. C. Shin, J. Hu, J. Hong, S. Jung, S.-H. Kim, K. Kim, D. Na, S. S. Park *et al.*, Construction and commissioning of PAL-XFEL facility, Appl. Sci. **7**, 479 (2017).

[63] A. Van Oosterom and J. Strackee, The solid angle of a plane triangle, IEEE Trans. Biomed. Eng. **BME-30**, 125 (1983).

[64] J. D. Jackson, *Classical Electrodynamics*, 3rd ed. (John Wiley & Sons, Inc., Hoboken, New Jersey, USA, 1998).

[65] Air linear absorption coefficient, https://henke.lbl.gov/tmp/xray4167.dat, accessed: 2020-06-10.

[66] Pt linear absorption coefficient, https://physics.nist.gov/cgi-bin/ffast/ffast.pl?Z=78&Formula=&gtype=5&lower=&upper=&density=&frames=no, accessed: 2020-06-10.

[67] Si_3N_4 linear absorption coefficient, https://physics.nist.gov/cgi-bin/ffast/ffast.pl?Formula=Si3N4&gtype=5&lower=&upper=&density=3.17, accessed: 2020-06-10.

[68] P. J. Brown, A. G. Fox, E. N. Maslen, M. A. O'Keefe, and B. T. M. Willis, Intensity of diffracted intensities, in *International Tables for Crystallography Volume C: Mathematical, Physical and Chemical Tables* (Springer Netherlands, Dordrecht, 2004).

[69] C. Kittel, *Introduction to Solid State Physics* (Wiley, New York, 2014).

[70] H. B. Michaelson, The work function of the elements and its periodicity, J. Appl. Phys. **48**, 4729 (1977).

[71] D. W. Lynch and W. Hunter, Comments on the optical constants of metals and an introduction to the data for several metals, in *Handbook of Optical Constants of Solids*, edited by E. D. Palik (Academic Press, Burlington, 1997).

[72] Electron-phonon coupling and electron heat capacity in metals at high electron temperatures, https://compmat.org/electron-phonon-coupling/, accessed: 2020-09-30.

[73] J. W. Arblaster, The thermodynamic properties of platinum, Platin. Met. Rev. **49**, 141 (2005).

[74] T. Ishikawa, J. T. Okada, P.-F. Paradis, and Y. Watanabe, Measurement of spectral emissivity and constant pressure heat capacity of liquid platinum with an electrostatic levitator, J. Chem. Thermodyn. **112**, 7 (2017).

[75] G. A. Slack, Platinum as a thermal conductivity standard, J. Appl. Phys. **35**, 339 (1964).

[76] S. Mehmood, U. E. Klotz, and G. Pottlacher, Thermophysical properties of the platinum-copper system, in *EPD Congress 2011* (John Wiley & Sons, Inc., Hoboken, New Jersey, USA, 2011).

[77] Q. G. Zhang, X. Zhang, B. Y. Cao, M. Fujii, K. Takahashi, and T. Ikuta, Influence of grain boundary scattering on the electrical properties of platinum nanofilms, Appl. Phys. Lett. **89**, 114102 (2006).

[78] R. E. Bedford, G. Bonnier, H. Maas, and F. Pavese, Recommended values of temperature on the International Temperature Scale of 1990 for a selected set of secondary reference points, Metrologia **33**, 133 (1996).

[79] J. W. Arblaster, Vapour pressure equations for the platinum group elements, Platin. Met. Rev. **51**, 130 (2007).

[80] M. Olbrich, E. Punzel, P. Lickschat, S. Weißmantel, and A. Horn, Investigation on the ablation of thin metal films with femtosecond to picosecond-pulsed laser radiation, Phys. Procedia **83**, 93 (2016).

[81] J. W. Arblaster, Selected electrical resistivity values for the Platinum Group of metals part I: Palladium and platinum, Johns. Matthey Technol. Rev. **59**, 174 (2015).